Reflection of vortex rings at a water-air interface

Zhuang Su [1,*] Christiana Mavroyiakoumou [2,†] and Jun Zhang [1,2,3,‡]
[1] NYU-ECNU Institute of Physics, New York University Shanghai, Shanghai 200124, China
[2] Applied Math Lab, Courant Institute, New York University, New York, New York 10012, USA
[3] Department of Physics, New York University, New York, New York 10003, USA

(Received 10 March 2025; accepted 20 June 2025; published 21 July 2025)

We experimentally investigate how vortex rings, generated and propagating within a water tank, interact with the water-air interface. Near-perfect reflections of these vortex rings occur when they approach the interface at a sufficiently large incident angle. To understand this interaction, we employ a vortex-sheet-vortex-pair model in numerical simulations, which captures the essential dynamics. Additionally, a simplified model based on the conservation of flux or momentum provides further insight into the mechanism behind the vortex-ring reflection. Through combined approaches—experimentation, numerical simulation, and detailed analysis—we gain a deeper understanding of how vortex rings interact with free boundaries.

DOI: 10.1103/dg4m-hbts

I. INTRODUCTION

Since Helmholtz first introduced the equations for vortex rings in 1858 [1], related problems have fascinated both mathematicians and physicists. Perhaps the most famous and immediate follower was Lord Kelvin, who was introduced to Helmholtz's work by his colleague Tait [2]. Amazed by the experiments performed by Tait on smoke rings, Lord Kelvin proposed his theory of vortex atoms [3] in which the idea of knotted vortices was introduced to explain the different structures between atoms. Although this theory was eventually abandoned as an atomic theory by Lord Kelvin himself [4] and his contemporaries, partly due to the discoveries in experimental atomic physics around the turn of the 20th century, the original idea and its theoretical interest persist to this day. For one, the topological concept of knots continues to attract attention across various fields, including electromagnetism [5,6] and fluid dynamics [7–9]. Additionally, knot theory has also developed into a key branch of modern topology [10–12]. Another line of research has focused on vortex dynamics, particularly the circular vortex ring. In Lord Kelvin's model, it represents the hydrogen atom as a zero knot and also bears similar importance in fluids. The evidence for the importance of vortex rings is ample. A vortex ring has been shown to serve as the building block of homogeneous and isotropic turbulence [13]. Its interactions with other vortex rings are also believed to play an important role in turbulence cascade [14], not to mention its ubiquity in flows observed in nature [15–19]. More recently, vortex structures, often known as toroidal vortices, have been created and detected in electromagnetic fields as well [20,21].

Northrup was one of the earliest researchers to continue the research on vortex dynamics [22,23]. He conducted a series of experiments in 1911 on vortex rings, covering a variety of phenomena including the collision and merging of two rings, as well as the reflection and refraction of a single

*Contact author: suz@nyu.edu
†Contact author: cm4291@cims.nyu.edu
‡Contact author: jun@cims.nyu.edu

ring at the interface of two fluids. Although the results were mostly qualitative, he confidently stated in his work: “The experiments which are about to be described would, if made earlier, have possibly had a greater interest as bearing upon Lord Kelvin’s ingenious theory of the vortex atom” [22]. Since then, many researchers have contributed in this direction, either on the dynamics of an isolated ring [24–32], on the interactions between rings [33–37], or on the interaction between vortex rings and boundaries, either solid or freely deformable fluid-air interfaces [38–40].

In particular, the coupling between vortex rings and deformable interfaces is complex, making the study of their interactions both mathematically challenging and physically intriguing. Related experiments become essential. Willmarth *et al.* [41] performed an experiment of a vortex pair moving vertically upwards toward the free surface and found that the vortex dissipates at the interface. Bernal and Kwon [42] produced a vortex ring that travels parallel to the surface and found that the top of the vortex ring opens up and reconnects to the surface, forming a U-shaped ring. Various observations have been made over the past decades, either from experimental or numerical studies. Their key findings are summarized in Table I. Three main types of phenomena have been observed: (1) the vortex ring dissipates beneath the interface, (2) the vortex ring opens up and reconnects to the interface forming a U-shaped ring, known as reconnection, and (3) the vortex ring moves across the interface. In the first two cases, the original vortex ring breaks up and dissipates after the interaction, whereas in the third case, the vortex ring rises entirely above the surface, and then collapses.

Surprisingly, the phenomenon of a vortex ring reflecting at the water-air interface, as reported by Northrup [22], did not draw much attention for an extended period of time, aside from some discussions that appeared in the work by Ohring and Lugt [43] and a few public videos online [44]. In contrast, the reflection of a vortex ring on a moving solid boundary has been reported by Chu and Falco [45], while Kuehn *et al.* [46] have reported vortex ring reflections at a gravity-induced interface separating two fluids with different densities. Similarly, numerical simulations have also demonstrated that in a superfluid, a quantum vortex dipole can reflect at an interface between regions of different densities [47]. Therefore, this study aims to advance the pending understanding of the reflection of a vortex ring at the water-air interface through experiments, numerical simulations, and simple modeling.

Focusing on an isolated vortex ring, the Reynolds number $\mathrm{Re} = \Gamma/\nu$ predominantly determines its dynamics, where Γ is the circulation of the vortex ring, which is the line integral of fluid velocity around the vortex, and ν is the kinematic viscosity. However, upon a freely deformable water-air interface, the behavior of a vortex depends on the competition between its inertia and the gravitational force, which limits the vertical motion of a vortex ring that tends to cross the interface. The two competing factors form a dimensionless parameter known as the Froude number, defined as $\mathrm{Fr} = \Gamma/\sqrt{gL_0^3}$, where L_0 is the diameter of the vortex ring and g is the gravitational constant. In addition to Fr, another key parameter that affects the dynamics is the incident angle θ_i at which the vortex ring aims at the interface.

By examining a wide range of Fr and θ_i, the current research rediscovers and confirms that a vortex ring undergoes near-perfect reflection at a water-air interface, depending on the incident angle, in a way similar to the total internal reflection (TIR) of light in optics. Most importantly, a phase diagram of the related phenomena in the $\mathrm{Fr} - \theta_\mathrm{i}$ space is unveiled through systematic experiments. In comparison, we report results from a detailed numerical simulation that captures the essential dynamics. The phase diagram, found through simulations, is consistent with the experimental findings. A much simplified model, which focuses on the conservation of mass and momentum, also provides some physical insights that help explain the reflection.

The rest of our work is structured as follows. Section II introduces the experimental setup and the basics of a vortex ring. Section III provides the experimental results and their analysis. Section IV discusses a numerical model, and the simulation results are placed in Sec. V. Section VI introduces the simplified model. Lastly, Sec. VII is the discussion and conclusions.

TABLE I. Key results and their typical parameter ranges for the Froude number Fr, incident angle θ_i, and Reynolds number Re used in previous computational (^{c}), experimental (^{e}), and theoretical (^{t}) studies, presented in chronological order. A vortex ring reflection at a free surface was first observed in 1911 by Northrup [22] (with the estimated parameters listed), but was largely forgotten for over a century. The current study unveils most of the phenomena found in the list. In the Fr column, the markers 2D or 3D show whether the definition of Fr is based on a 2D or 3D framework. The distinction between the two is discussed in Sec. V. The "√" symbol indicates which vortex ring behaviors were reported in each study. In the "dissipated" column, the "$\surd_R$" symbol shows which studies observed vortex rings undergoing reconnection. "Reflected" is shown in bold font to emphasize its importance in the current study.

Reference	Fr	θ_i (deg)	Re	Observed result			
				Dissipated	**Reflected**	Broken	Across
Northrup (1911) [22]^{e}	3.7 (3D)	"Small," 65–90	30 000		√		√
Telste (1989) [48]^{c,t}	0.5, 2.24, 7.07 (2D)	0	—	√			√
Willmarth *et al.* (1989) [41]^{c,e}	2.47 (2D)	0	3000	√			
Bernal and Kwon (1989) [42]^{e}	0.41 (3D)	90	7400	$\surd_R$			
Bernal *et al.* (1989) [49]^{e}	0.1, 1.45 (3D)	0	2500, 3800, 18 000	√			
Yu and Tryggvason (1990) [50]^{c}	0.5–22.4 (2D)	0, 45	—	√			√
Song *et al.* (1992) [51]^{e}	0.252–0.988 (3D)	0	15 100–64 700	√$\surd_R$			
Lugt and Ohring (1994) [52]^{c}	0.01, 0.2 (3D)	45	100	√$\surd_R$			
Wu *et al.* (1995) [53]^{c}	0.707, 7.07 (3D)	0	1000	√			√
Weigand and Gharib (1995) [54]^{e}	0.46 (3D)	70–83	7500	$\surd_R$			
Ohring and Lugt (1996) [43]^{c}	0.01, 0.08, 0.2 (3D)	45, 70	100, 200	√$\surd_R$			
Gharib and Weigand (1996) [55]^{e}	0.07, 0.2 (3D)	83	1150, 5000	$\surd_R$			
Zhang *et al.* (1999) [56]^{c}	0, 0.166 (3D)	60, 70, 80	471, 942, 1570	$\surd_R$			
Archer *et al.* (2010) [57]^{c}	0 (3D)	0	3708, 7417, 11 126	√			
Current study^{c,e,t}	0.45–2.6 (3D)	40–90	3400–23 000	√$\surd_R$	√	√	√

II. VORTEX RING GENERATION AND ITS BASIC PROPERTIES

Vortex rings in our experiment are generated in water via a spring-loaded piston system as sketched in Fig. 1(a). The releasing speed and displacement of the piston are controlled by a stepper motor through a steel cable pulling at the rear end. The nozzle outlet diameter of the vortex generator is 1.5 cm. This generator is submersed in a water tank with a 1 × 1 m footprint and a height of 0.5 m

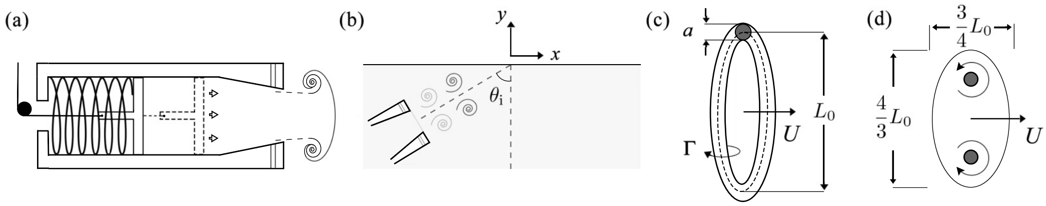

FIG. 1. Vortex generator and vortex ring. (a) Vortex generator: a spring-loaded piston, released at controlled speed and distance, pushes a volume of fluid out from a tapered (10°) opening (1.5 cm diameter). The accelerated fluid forms a vortex ring that travels forward. (b) Aiming at the free surface with an incident angle θ_i, a vortex ring moves towards the water-air interface and interacts with it. (c) Sketch of the vortex core that propagates at speed U with circulation Γ. The vortex ring has a diameter L_0, with its vorticity concentrated near the core of diameter a. (d) A volume of fluid is entrained around the core and moves forward. The ellipsoid "bubble" is the average shape of vortex rings uncovered using streamlines measured by particle image velocimetry (PIV).

that is filled up to 0.4 m. By varying the release speed and displacement of the piston, vortex rings of different strengths can be generated, thereby altering the Froude number Fr. Changing Fr is equivalent to changing Re here since they only differ by a constant as the vortex diameter is fixed at approximately 1.9 cm in this study. A small amount of fluorescent dye is pre-injected from both the top and bottom near the nozzle outlet, where the dye stays put until the piston is released. As the vortex ring forms, the fluorescent dye rolls up into the top and lower portions of the ring, marking only two representative locations of the 3D structure. For later convenience, we refer to the upper and lower portions of the same vortex ring as the upper and lower cores, respectively, as shown in the following text and images. The vortex cores are then captured by a high-speed camera, iX i-SPEED 211, at a frame rate of up to 1000 fps with a field-of-view size of about 8 cm × 20 cm. The trajectories of the cores are tracked with an object-tracking algorithm, and the core velocities are subsequently obtained. The vortex ring generator is mounted on a rotational stage, which makes it convenient to adjust the incident angle θ_i [Fig. 1(b), simplified]. For each experiment run, the generator is fixed at a specific incident angle, then the vortex ring is released and recorded until it exits the field of view of the camera.

A. The vortex ring and its effective drag coefficient

The vorticity of a vortex ring concentrates in a circular ring of diameter L_0 with a core diameter a, as shown in Fig. 1(c). Surrounding the vortex core, a blob of fluid is entrained and moves along, creating a vortex bubble, as depicted in Fig. 1(d). The circulation Γ of a vortex ring in an ideal fluid is conserved [58], allowing it to maintain a constant propagation speed U. However, for a viscous vortex ring, its energy is continuously dissipated, causing it to slow down. In the early stage, shortly after the vortex ring is formed, the entrainment of the ambient fluid is weak [59], and the size of the vortex bubble can be considered constant. The shape of the vortex bubble is approximated as an ellipsoid based on the streamlines surrounding its boundary [60], as shown in Fig. 2(a). The streamlines are constructed using the particle image velocimetry (PIV) measurements. The length of the major and minor axes of the ellipsoid are found to be $4L_0/3$ and $3L_0/4$ within a 10% error for the vortex rings studied here. This gives a ratio of approximately 0.56 between the minor and major axes. Similar values ($0.55 \sim 0.63$) have also been reported in previous studies [32,61,62], demonstrating shape similarity between vortex rings of different sizes and speeds. Given its ellipsoid shape, the volume of the vortex bubble is estimated to be $V = 2\pi L_0^3/9$.

Since the vortex bubble has little material exchange with its surroundings, we treat the moving vortex as a bluff body and compute its effective drag coefficient. In particular, the drag coefficient is $C_d = 2F_d/\rho U^2 A$, where F_d is the drag force, $A = 4\pi L_0^2/9$ is the flow-facing area, and ρ is the fluid

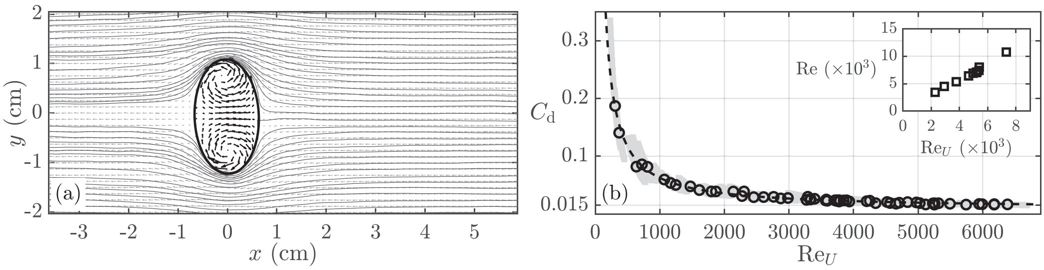

FIG. 2. A vortex bubble and its effective drag coefficient. (a) Flow field and streamlines around an advancing vortex ring, in a coordinate fixed at the ring center, measured by PIV. The thick black ellipse marks the boundary of the volume shown in Fig. 1(d). (b) Drag coefficient C_d of vortex rings versus Re_U. The circles show the drag coefficients of a vortex ring based on its speed and deceleration, and each gray band shows how the drag coefficient evolves over time as a vortex ring slows down (Re_U decreases). The dashed line shows the relationship fitted by Eq. (1). The inset shows the relationship between Re and Re_U.

density. The drag force F_d is defined as $F_\mathrm{d} = \rho V a_r$, which is the product of the mass of the vortex bubble and the deceleration a_r derived from the core velocities. This gives a drag coefficient of $C_\mathrm{d} = a_r L_0/U^2$. Figure 2(b) shows the dependence of the drag coefficient on the Reynolds number, $\mathrm{Re}_U = 4UL_0/3\nu$, defined based on the bubble diameter and its propagation speed. The relationship between Re_U and Re is given in the inset of Fig. 2(b). For the vortex rings examined in this study, $\mathrm{Re} \simeq 1.5\mathrm{Re}_U$. The experimental data is fitted to show that C_d depends on Re_U, following an empirical relationship over the range $300 < \mathrm{Re}_U < 7000$:

$$C_\mathrm{d} = \frac{260}{\mathrm{Re}_U^2} + \frac{53.4}{\mathrm{Re}_U} + 0.0088. \tag{1}$$

The drag coefficient of a vortex ring is extremely small, as low as 0.017 at $\mathrm{Re}_U \sim 6500$, compared to that of a solid body of a similar shape, which is normally greater than 0.5 [63]. A similar definition of drag coefficient has also been used in previous works [32,60,64,65] and limited results have been reported. For vortex rings with Reynolds numbers below 300, the drag coefficient reported by Sullivan *et al.* [32], when converted to the current definition, ranges from approximately 0.2 to 3. Gan *et al.* [60] reported drag coefficient values of 0.33 and 0.4 for turbulent vortex rings with Reynolds numbers of 41 280 and 20 039, respectively. The huge difference, of almost two orders of magnitude, between their drag coefficients [32,60] and our values, is due to the different Re_U ranges (low vs high) and states of motion (turbulent vs laminar) at which the numbers are measured. Evidenced by our results shown in Fig. 2(b), C_d rapidly increases at low Re_U due to significant viscous dissipation. Similarly, dissipation across scales in a turbulent vortex ring quickly slows the vortex motion, leading to higher drag coefficients. In our experiments, when $\mathrm{Re}_U \geqslant 5000$, the speed drop for the vortex rings is around 10% of the initial speed over a distance of $8L_0$. Thus, in the current study, the propagation speed of vortex rings at high Reynolds numbers is considered constant.

III. EXPERIMENTAL RESULTS AND DISCUSSION

The following ranges of Froude number and incident angle are tested: $\mathrm{Fr} \in [0.45, 2.6]$ and $\theta_\mathrm{i} \in [40^\circ, 85^\circ]$. The parameter ranges are so chosen to include large Fr and θ_i cases that were often overlooked by previous works (Table I). This expanded parameter range makes it possible to observe a broader range of phenomena, including vortex ring reflection, documented by Northrup in 1911 [22].

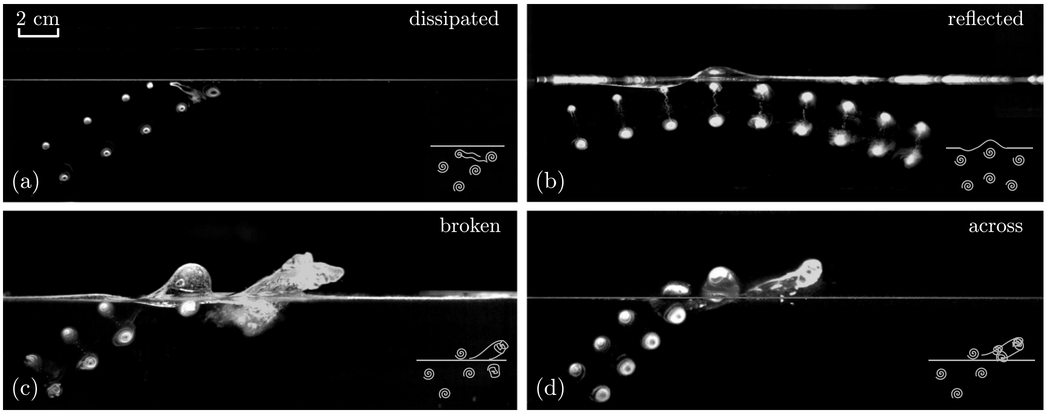

FIG. 3. Vortex rings that interact with a water-air interface exhibit four behaviors. Each case is shown with snapshots, pulled from high-speed video recordings, taken at equal time intervals of 0.25, 0.04, 0.04, and 0.04 seconds, respectively. The scale in the four images is the same. The vortex ring (a) dissipates near the water-air interface; (b) reflects while temporarily deforming the interface ($\theta_i = 75^\circ$); (c) breaks at the interface (upper portion moves above the interface and the whole ring breaks up); and (d) crosses the interface (the entire core of the ring moves above the interface) and then forms a jet. The insets on the bottom right of each panel illustrate the behaviors. The interface is visualized using commercial baby powder, but all other measurements are conducted without the powder to ensure accuracy and to eliminate any possible influence on the results. For the complete movies see the Supplemental Material [66].

A. Four types of behavior and the phase diagram

Four types of behavior are observed in the current experiments, shown by typical examples in Fig. 3. In the "dissipated" case shown in Fig. 3(a), when Re is low, the vortex ring can hardly deform the interface and its structure is destroyed and dissipated near the interface due to viscous effects. The "reconnection" phenomenon, where the top part of the vortex ring opens up and connects to the interface, is also observed. It is, however, classified as a "dissipated" state here as the structure of the original vortex ring is destroyed upon interaction. In the "reflected" case shown in Fig. 3(b), the vortex ring notably deforms the interface, causing its propagation direction to deflect downward, resulting in a reflection while preserving its original structure. For the "broken" and "across" cases shown in Figs. 3(c) and 3(d), where θ_i is smaller, the propagation direction of the vortex ring also deflects downward as it approaches the interface, similar to the "reflected" case. However, in these two cases, the vortex ring travels too far beyond the interface for it to reflect. If the entire ring moves above the interface, it forms a jet in the air and soon collapses. This is classified as an "across" case. If the ring does not move fully above the interface, the portion above the interface breaks up and smashes the remaining portion underneath. It is then termed a "broken" case, which is an intermediate situation between reflection and across cases. Indeed, the difference between the last two cases [Figs. 3(c) and 3(d)] is small, and distinguishing them can be challenging at times. But the differences between the "dissipated," "reflected," and "broken and across" cases are evident.

To compare the four above cases in the parameter space of Froude number (or, equivalently, the Reynolds number) and incident angle, a phase diagram is constructed based on systematic experiments, as shown in Fig. 4. When Fr is less than a critical value $\mathrm{Fr_c}$ of approximately 1, the interface deformation is small and the vortex ring dissipates regardless of the incident angle θ_i. This state is marked as regime I, corresponding to the "dissipated" behavior. For $\mathrm{Fr} \geqslant \mathrm{Fr_c}$, the vortex ring carries greater momentum that can visibly deform the interface, leading to the three other behaviors. For θ_i smaller than a critical value θ_c, the vortex ring may either cross the interface or break up upon contact, as shown by regime III, which corresponds to "across" or "broken" cases. The critical value θ_c has been found to locate in a finite range, between 53° and 55°. In regime III,

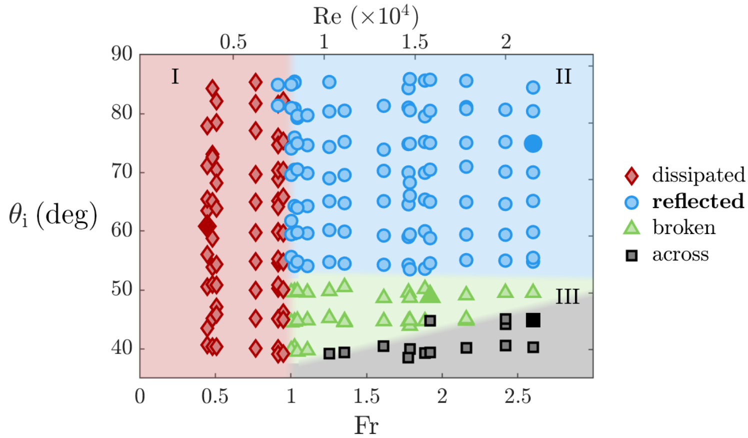

FIG. 4. Phase diagram of the vortex-interface interaction, in Fr $-$ θ_{i} or, equivalently, in Re $-$ θ_{i} space. The phase diagram is divided into three regimes (I, II, and III) by a critical Froude number Fr_{c} and a critical incident angle θ_{c}. Below Fr_{c}, vortex rings are dissipated, no matter what θ_{i} is. Above Fr_{c}, however, larger θ_{i} gives rise to reflection and lower θ_{i} yields broken and across cases. The four solid, larger markers correspond to cases shown in Fig. 3.

the behavior is influenced by θ_{i} and Fr. At higher momentum (higher Fr or Re) and smaller incident angle, vortex rings are more likely to cross than to break up at the interface. For regime II, when both Fr and θ_{i} exceed the critical values, the vortex ring bounces robustly off the interface, which corresponds to the "reflected" behavior. In this regime, the interaction exhibits weak dependence on Fr or Re, as the trajectories of vortex rings with the same θ_{i} but different Fr show minor differences. The phenomenon shown by regimes II and III, where reflection can occur only at sufficiently large incident angles, closely resembles the total internal reflection of light in optics. Moreover, if the vortex rings can survive above the interface, the "across" cases may be interpreted as "refracted." This scenario where the vortex ring can survive beyond the interface has previously been discussed in the context of sharply stratified density interfaces, where the vortex ring can cross the interface and remain coherent [46,67–70]. With the phase diagram in place, the following discussion focuses on the "reflected" regime.

B. Reflection of vortex rings

Figure 5(a) shows a typical reflection process of a vortex ring at the interface when $\mathrm{Fr} = 1.92$ and $\theta_{\mathrm{i}} = 70^{\circ}$. If the vortex ring is far from the interface, it travels along a straight line in the upper-right direction. As it approaches the interface, the ring begins to rotate clockwise, causing its trajectory to deflect downward. After reaching its highest point, the ring continues to rotate and deflect, altering its propagation direction to the lower right direction. Once it moves far enough from the interface, the rotation stops and the vortex ring resumes its straight path. It is evident that the continuous rotation and reorientation of the vortex ring are key to its reflection. The evolution of the propagation angle of the vortex ring, $|\theta(x)|$, as defined in the inset, is plotted in Fig. 5(c). In each case, $|\theta(x)|$ starts with the incident angle θ_{i} and increases to 90° as the vortex ring reaches the apex—at which instant the vortex ring moves horizontally—then decreases back to the value of the reflection angle θ_{i}^{*}, completing the reflection. The reflection angle is slightly less than the incident angle, but the curves of the propagation angle are essentially symmetric, and the reflection angles change monotonically with their incident angles, demonstrating a robust reflection mechanism. Data points are averaged over five repeating runs for each θ_{i}. The error bars show the standard deviation of $|\theta(x)|$.

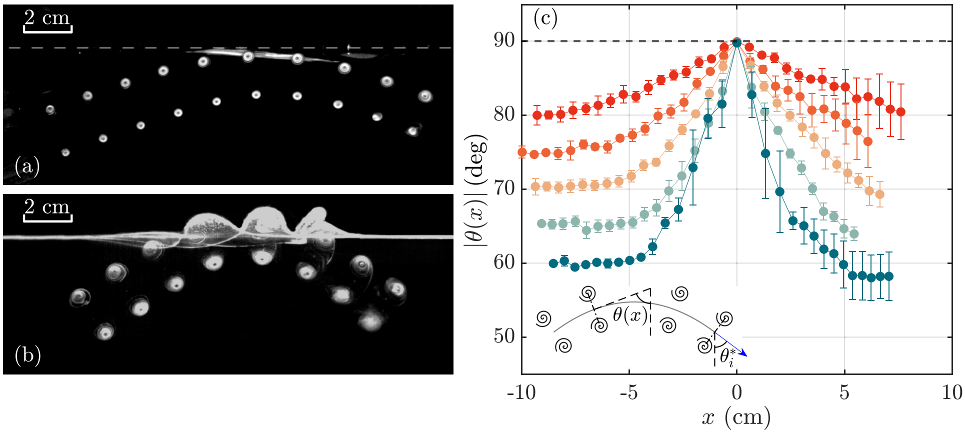

FIG. 5. Vortex ring reflection at the interface, when Fr = 1.92 and θ_i is (a) 70° and (b) 55°. The dashed line in panel (a) shows the unperturbed interface while the deformed interface is not visualized. For a complete movie, see the Supplemental Material [66]. (b) Deformed interfaces visualized at snapshots 4, 5, and 6, respectively. The vortex ring structure is well preserved after the reflection even though a large part of the vortex ring has moved above the interface. This is a "borderline" case in reflection, but close to a "broken" case. (c) The evolution of $|\theta(x)|$ when Fr = 2.6 and θ_i is between 60° and 80°. $|\theta(x)|$ evolves from θ_i to 90° and then drops back during the reflection, showing the rotation of the ring. The inset shows the definition of $\theta(x)$ and the reflection angle θ_i^*.

The rotation of the ring is achieved by the upper core moving faster in the horizontal direction than the lower core. As shown in Figs. 6(a) and 6(b), before reaching close to the interface, both the upper and lower cores have the same horizontal and vertical velocities u_x and u_y. When close to the interface, the horizontal velocity of its upper core significantly increases, surpassing that of the lower core, while their vertical velocities remain equal. This velocity difference drives the vortex-ring reorientation and ultimately leads to reflection. For comparison, the horizontal velocity component of the entire ring, expressed as $U_0 \sin\theta(x)$, is plotted. Here U_0 is the average speed of the two cores during straight-line motion. $U_0 \sin\theta(x)$ increases as the vortex ring begins to rotate, reaches a maximum at $\theta(x) = 90°$, and then decreases back. During reflection, the horizontal velocity of the lower core is closely in line with $U_0 \sin\theta(x)$, showing that the lower core is not accelerated. After reflection, as we observe, the horizontal velocities of both cores decrease from $U_0 \sin\theta(x)$ by approximately 10%. This reduction in speed and energy is attributed to the viscous dissipation as the vortex ring travels and to the energy spent creating surface deformations. Note that the diameter of the vortex ring also slightly decreases as a result of reduced kinetic energy. Figure 6(b) shows the vertical velocity components of the two cores, which are both close to $U_0 \cos\theta(x)$, following the same trend. After reflection, the reduced horizontal speed and fully restored vertical speed result in a slightly smaller reflection angle, which is consistent with the $\theta(x)$ measurement in Fig. 5(c).

The acceleration effect induced by the interface on the upper core is observed to intensify with decreasing incident angle. This is shown by the maximum horizontal velocity difference $\Delta\hat{u}_x$ plotted against θ_i in the inset of Fig. 6(a). Another relevant quantity is the depth of reflection h, defined as the distance between the flat interface and the highest position that a vortex ring can reach, as shown by the inset of Fig. 6(c). The black squares in there show that a vortex ring with a smaller incident angle reaches closer to or even goes above the flat interface. The proximity to the interface is found to yield a stronger acceleration on the upper core. For a 3D vortex ring, such an effect is conceivably weaker on portions of the ring gradually away from the top and weakest on the lower portion of the ring. However, this acceleration effect has its limit. If the ring fails to complete the rotation before it rises too far above the interface when the incident angle is below a certain value (θ_c), the vortex

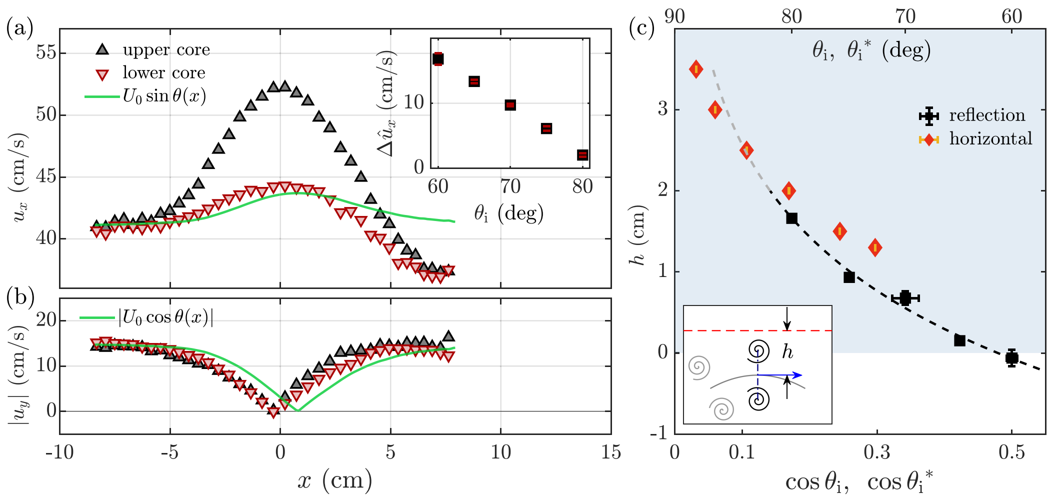

FIG. 6. The velocity decomposition and reflection depth h. (a, b) The horizontal and vertical velocity components of the upper and lower cores are compared, also with those of the entire vortex ring, expressed as $U_0 \sin\theta(x)$ and $U_0 \cos\theta(x)$, respectively, when Fr $= 1.92$ and $\theta_i = 70°$. The inset in panel (a) shows that the peak horizontal velocity difference, $\Delta\hat{u}_x$, between the two cores decreases with increasing θ_i. (c) The reflection depth h (defined in the inset) decreases with decreasing θ_i. When vortex rings are issued horizontally ($\theta_i = 90°$), red symbols show the reflection angles θ_i^* decrease with decreasing depth of release (also denoted as h). The dashed curve is fitted from the reflection data.

ring ends up with a "broken" or "across" case. That is to say, the critical incident angle for the reflection is the result of the interplay between the rotation and the vertical motion of the vortex ring. Figure 5(b) shows a "borderline" case at $\theta_i = 55°$, in which a large portion of the ring rises above the interface as if a jet is about to form and break the ring below, yet the ring is still reflected.

Interestingly, when vortex rings are generated horizontally ($\theta_i = 90°$)—close to the interface at an initial depth—they are also deflected downward by the interface. Figure 7 shows two examples with different initial depths: (a) 1.5 cm and (b) 2.5 cm, both at Fr $= 1.92$. The deflection is more significant when the initial depth is smaller. In addition, the trajectory of a horizontally issued vortex ring closely resembles that of the outgoing part of a reflected ring. The apparent equivalence between the initial depth of a vortex ring issued parallel to the interface and the depth of reflection for an ascending ring leads us to denote both quantities by the same parameter h. For the horizontally issued vortex rings, when $\theta_i = 90°$, h is called the depth of release. Similarly, the reflection angle θ_i^* is used for the horizontal cases as well. The diamond symbols in Fig. 6(c) show that θ_i^* decreases

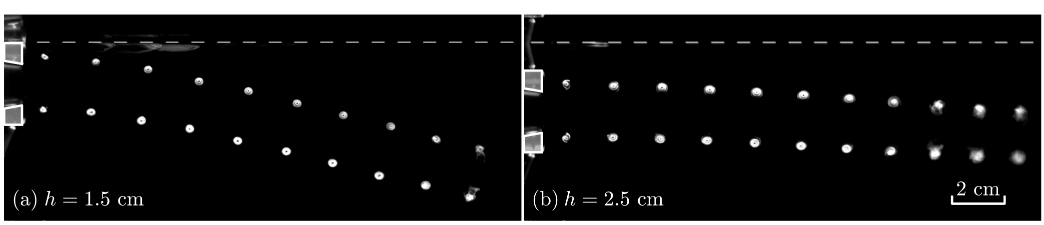

FIG. 7. Vortex rings issued parallel to the interface ($\theta_i = 90°$) at Fr $= 1.92$, with (a) $h = 1.5$ cm and (b) $h = 2.5$ cm. The deflection is stronger in (a) when h is smaller than that in (b). The scale in the two images is the same. The nozzle of the vortex generator is highlighted on the left in both images.

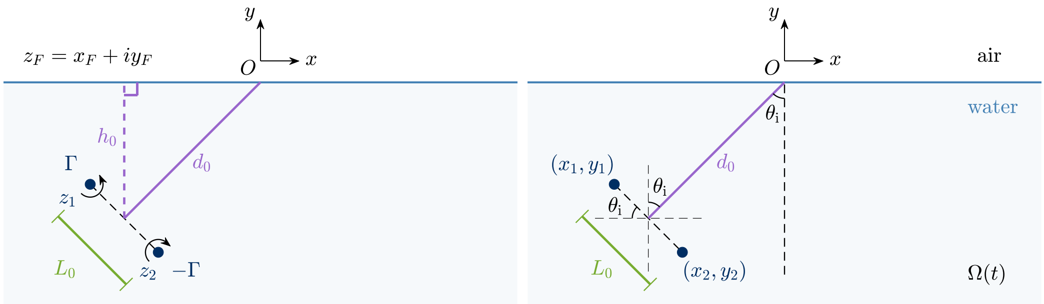

FIG. 8. Vortex sheet and vortex pair model initial setup. The two dark dots represent a pair of point vortices of equal strength but opposite sign, Γ and $-\Gamma$, located a distance L_0 apart at $z_1 = x_1 + iy_1$ and $z_2 = x_2 + iy_2$, with a depth h_0 and inclined depth d_0. The location of the free water-air interface is denoted by $z_F = x_F + iy_F$ and the incident angle by θ_i.

as h decreases. Compared to the reflection cases, the relationship between θ_i^* and h for horizontal rings exhibits a similar trend to that of θ_i vs h.

C. Vortex interactions with a fixed wall

The interactions between a vortex ring and a fixed wall are also investigated to show the significance of Fr for reflection. Lim [39] has shown that as a vortex ring approaches a solid wall obliquely, its vortex cores split up, with the lower portion of the ring slightly rebounding before the vortex ring vanishes. This behavior mirrors the “dissipated” cases observed in our experiments, where the weak vortex ring lacks sufficient energy to induce significant water-air interface deformation. In contrast, in the solid boundary scenario, the rigidity of the wall prevents the vortex ring from inducing any deformations. This is equivalent to $\mathrm{Fr} = 0$ for any vortex ring. That being stated, the interaction behavior of any vortex ring with a fixed wall falls into regime I in the $\mathrm{Fr} - \theta_i$ phase diagram (Fig. 4) regardless of the vortex strength and its incident angle. A direct comparison between the solid wall and water-air interface is presented in Fig. S1 in the Supplemental Material [66].

IV. VORTEX-SHEET-VORTEX-PAIR MODEL AND NUMERICAL METHOD

A 2D vortex-sheet-vortex-pair model is used to numerically simulate the interaction. In this model, the vortex ring is represented by a pair of point vortices with opposite circulations (Γ and $-\Gamma$), while the interface is modeled as a vortex sheet with distributed strength γ. Both the point vortices and the interface evolve freely under their mutual interaction. Surface tension is neglected here, as experimental observations show that the typical scale of surface deformation is comparable to the vortex diameter in the reflected cases. The Weber number can be used to characterize the relative importance of inertial forces to surface tension. Its definition is $\mathrm{We} = \Delta\rho\Gamma^2/(\sigma L_0)$, where $\Delta\rho$ is the density difference between water and air, and the surface tension coefficient of water is taken as $\sigma = 0.072\,\mathrm{N/m}$. With a vortex diameter L_0 of approximately 1.9 cm, the Weber number ranges from 8 to 400 for all vortex rings tested in the current experiments. Previous simulations that included surface tension have shown that it only becomes significant when the Weber number approaches unity [50,53]. Figure 8 illustrates the initial setup of the model. A semi-infinite domain $\Omega(t)$ is assumed beneath the interface $z_F = x_F + iy_F$, where the point vortices $z_1 = x_1 + iy_1$ and $z_2 = x_2 + iy_2$ are placed with an incident angle θ_i relative to the interface. The entire domain is assumed to be free of vorticity, except for where the point vortices and the interface are. The method employed was first proposed by Baker, Meiron, and Orszag [71], and was also used by Telste [48] to study vortex ring and water-air interface interactions. Here, building on these two works, small modifications to the method are made. The derivation is briefly repeated for the completeness of our work.

The vortex sheet strength γ and the position z_F of the interface are both parameterized by a Lagrangian coordinate e, $-\infty < e < \infty$ and time, $t \geqslant 0$ as $\gamma(e,t)$ and $z_F(e,t) = x_F(e,t) + iy_F(e,t)$, respectively. The flow is represented as the superposition of the potential flows induced by the interface and the two discrete point vortices [48,72,73]. The complex velocity potential $w(z)$ at $z = x + iy$ in the fluid domain $\Omega(t)$ is given by

$$w(z) = \frac{1}{2\pi i}\int_{-\infty}^{\infty} \gamma(e',t)\ln[z - z_F(e',t)]\,\mathrm{d}e' + \frac{1}{2\pi i}\ln(z - z_1) - \frac{1}{2\pi i}\ln(z - z_2). \tag{2}$$

This and all subsequent equations are nondimensionalized using the initial distance L_0 between the vortices in the pair as the characteristic length scale, with the timescale L_0^2/Γ, and the velocity scale Γ/L_0. The complex velocity $u_x + iu_y$ at points z inside the domain, except for where the vortex pair is, can be calculated as the conjugate of $\mathrm{d}w/\mathrm{d}z$:

$$u_x(z) - iu_y(z) = \frac{\mathrm{d}w}{\mathrm{d}z} = \frac{1}{2\pi i}\int_{-\infty}^{\infty} \frac{\gamma(e',t)}{z(e,t) - z_F(e',t)}\,\mathrm{d}e' + \frac{1}{2\pi i}\frac{1}{z - z_1} - \frac{1}{2\pi i}\frac{1}{z - z_2}. \tag{3}$$

The velocities $\mathrm{d}z_1/\mathrm{d}t$ and $\mathrm{d}z_2/\mathrm{d}t$ of the two point vortices are

$$\begin{aligned} \frac{\mathrm{d}\bar{z}_1}{\mathrm{d}t} &= \frac{1}{2\pi i}\int_{-\infty}^{\infty} \frac{\gamma(e,t)}{z_1(t) - z_F(e,t)}\mathrm{d}e - \frac{1}{2\pi i}\frac{1}{z_1 - z_2}; \\ \frac{\mathrm{d}\bar{z}_2}{\mathrm{d}t} &= \frac{1}{2\pi i}\int_{-\infty}^{\infty} \frac{\gamma(e,t)}{z_2(t) - z_F(e,t)}\mathrm{d}e + \frac{1}{2\pi i}\frac{1}{z_2 - z_1}, \end{aligned} \tag{4}$$

respectively [48]. Since the integral in Eq. (3) is singular on the interface, it cannot give the velocity of the interface directly. Instead, a Cauchy-principal-value integral is applied to give the interface velocity q as

$$\bar{q} = \frac{1}{2\pi i}\,⨍_{-\infty}^{\infty} \frac{\gamma(e',t)}{z_F(e,t) - z_F(e',t)}\,\mathrm{d}e' + \frac{1}{2\pi i}\frac{1}{z_F - z_1} - \frac{1}{2\pi i}\frac{1}{z_F - z_2}. \tag{5}$$

Also, a constant weight factor α is introduced to give better control on the interface velocity. Thus, the actual velocity used in the model is

$$\frac{\partial \bar{z}_F(e,t)}{\partial t} \equiv \bar{Q}(e,t) = \bar{q}(e,t) + \frac{\alpha}{2}\frac{\gamma(e,t)}{\partial_e z_F(e,t)}. \tag{6}$$

The weight factor α, $-1 \leqslant \alpha \leqslant 1$, determines the weighting of the potential from both sides of the interface; the velocity is that of the lower fluid when $\alpha = 1$ and that of the upper fluid when $\alpha = -1$. A detailed derivation of Eq. (6) can be found in previous works [48,72].

To close the system, an evolution equation for $\gamma(e,t)$ is needed. For that, the Lagrangian form of the Bernoulli equation is introduced on the interface z_F as the dynamic boundary condition:

$$\frac{\mathrm{D}\phi}{\mathrm{D}t} = \frac{1}{2}\left[\left(\frac{\partial\phi}{\partial x}\right)^2 + \left(\frac{\partial\phi}{\partial y}\right)^2\right] - \frac{1}{(\mathrm{Fr})^2}y. \tag{7}$$

Here ϕ is the velocity potential, the real part of w. The derivation of the dimensionless Bernoulli equation [Eq. (7)] can be found in Sec. SII of the Supplemental Material [66]. The Froude number Fr that appears in the last term of Eq. (7) enters the evolution equation of the vortex sheet strength $\gamma(e,t)$ and acts as one of the dominant parameters that affect the dynamics. For a water-air interface, the evolution equation for $\gamma(e,t)$ is given by

$$\frac{\partial\gamma(e,t)}{\partial t} = \left(\frac{\alpha}{2} - \frac{1}{4}\right)\frac{\partial}{\partial e}\left[\frac{\gamma^2}{(\partial_e z_F)(\partial_e \bar{z}_F)}\right] - 2\left[\Re\left(\frac{\partial\bar{q}}{\partial t}(\partial_e z_F)\right) - \frac{\alpha}{2}\gamma\Re\left(\frac{\partial_e q}{\partial_e z_F}\right) + \frac{1}{(\mathrm{Fr})^2}\partial_e y_F\right]. \tag{8}$$

Equation (8) is derived in Sec. SIII of the Supplemental Material [66]. Shelley and Vinson [74] have also derived an equivalent equation directly from the Euler equations and velocity boundary conditions at the fluid interface, without making any assumptions about the vorticity distribution within the fluid.

In the actual computation, the Cauchy-principal-value integral in Eq. (5) is replaced by a regularized integral to avoid short-wave instability [75,76]. With this instability occurring after a certain number of time steps, the interface would form a sawtooth shape and rapidly destabilize afterwards. The regularized integral takes the form

$$\frac{1}{2\pi i}\int_{-\infty}^{\infty}\gamma(e',t)\frac{\overline{z_F(e,t)-z_F(e',t)}}{|z_F(e,t)-z_F(e',t)|^2+\delta^2}\,\mathrm{d}e', \tag{9}$$

where δ is a regularization parameter. The effect of δ is to prevent the growth of free surface structures on scales that are smaller than δ, while maintaining the shape and motion of the vortex sheet on larger scales [74,75]. In the far-field $\mathbf{u}=0$ is enforced, which in potential flow $\mathbf{u}=\nabla\phi$ corresponds to

$$\frac{\partial\phi}{\partial x}=0 \quad \text{for} \;\; x=\pm\infty \;\; \text{in} \;\; (x,y)\in\Omega(t); \qquad \frac{\partial\phi}{\partial y}=0 \quad \text{for} \;\; -\infty<x<\infty, \;\; y=-\infty. \tag{10}$$

This is satisfied if $\lim_{e\to\pm\infty}\gamma(e,t)=0$. Since initially the free surface is assumed to be undisturbed, we have that at $t=0$ on the interface z_F: $\phi_{t=0}=0$ and $y_F|_{t=0}=0$.

The numerical approach employed is now briefly described. At each time step, the positions of the two discrete vortices in the vortex pair $z_1(t)$, $z_2(t)$, the interface position $z_F(e,t)$, and the vortex sheet strength $\gamma(e,t)$, are solved using Eqs. (4), (6), and (8), respectively. The initial conditions are

$$z_F(e,0)=x_F(e,0); \quad \gamma(e,0)=0; \quad z_k(0)=x_k(0)+iy_k(0), \quad \text{for} \;\; k=1,2, \tag{11}$$

with

$$x_k(0)=-d_0\sin\theta_\mathrm{i}\mp(L_0/2)\cos\theta_\mathrm{i}; \quad y_k(0)=-d_0\cos\theta_\mathrm{i}\pm(L_0/2)\sin\theta_\mathrm{i}, \tag{12}$$

where θ_i is the incident angle, d_0 is the initial inclined depth of the vortex pair, and L_0 is the initial distance between the vortices as shown in the schematic diagram in Fig. 8, which is nondimensionalized to 1.

Both the interface position $z_F(e,t)$ and the vortex-sheet strength $\gamma(e,t)$ are discretized spatially by defining

$$(z_F)_j(t)\equiv(x_F)_j(t)+i(y_F)_j(t)=z_F(e_j,t); \quad \gamma_j(t)=\gamma(e_j,t), \tag{13}$$

on a uniform grid with $e_j=j$ and $t\geqslant 0$, where $j=1,2,\ldots,N$ with N representing the grid size. The discretized initial conditions are thus given by $(z_F)_j(0)\equiv(x_F)_j(0)$ and $\gamma_j(0)=0$, where $(y_F)_j(0)=0$ for the initial flat interface. Since the free surface is infinitely long, a wave-damping-type procedure is adopted to perform the computations over a finite region [48,72]. In particular, the computations are done over a finite but large region $|x_F|\leqslant L$ with $L\gg L_0$. Specifically, $L=50$ with the damping terms applied to Eqs. (6) and (8) in regions of $|x_F|\geqslant 45$. The damping coefficient is set to 0.1. The weight factor that appears in the interface velocity [Eq. (6)] is chosen as $\alpha=-1$, which is the same as the value used by Telste [48]. Among different values of α, this choice produced the most desirable free-surface spacing in terms of resolution and uniformity. Further discussion about the role of α is included in Sec. SIII of the Supplemental Material [66].

For each discrete point j on the interface, $(z_F)_j(t)$ and $\gamma_j(t)$ from Eq. (13) satisfy the discretized versions of the coupled evolution equations [Eqs. (4), (6), and (8)]. Therefore, in total there are $3N+2$ equations in the full system of governing equations: N equations for each of the three evolution equations for the interface and two equations for each of the discrete point vortices comprising the vortex pair. The integral in Eq. (9) is computed using trapezoidal quadrature and the spatial derivatives with respect to the Lagrangian coordinate e are computed using fourth-order finite difference formulas. The evolution equation for the vortex sheet strength on the interface is solved iteratively by employing the generalized minimal residual (GMRES) method [77] (see Sec. SIV of the Supplemental Material [66] for details), and $\gamma(e,t)$ and $z_F(e,t)$ are obtained by integrating $\partial_t\gamma$ and $\partial_t z_F$ in time using a fourth-order Runge-Kutta method. The simulation results shown in Sec. V are with $N = 1000$ points on the free surface, time step $\Delta t = 10^{-3}$, and regularization parameter $\delta = 0.1$. This choice of δ was determined empirically, and it was checked that using slightly different values would not change the phase diagram obtained from the simulations. The initial vertical depth below the interface for the vortex pair is set to $h_0 = 3$. Therefore, as a function of the incident angle, the inclined depth d_0 shown in Fig. 8 is given by $d_0 = h_0/\cos\theta_\mathrm{i}$.

Due to the nature of the interaction, the initially equally spaced grid points $(z_F)_j$ either cluster or disperse in the deformed regions of the free interface. This causes the numerical error to grow rapidly, leading to convergence issues for the GMRES method. To address this problem, a self-adaptive redistribution of the grid points on the interface is implemented. A threshold arc-length distance Δs between two adjacent grid points is introduced. At each time step, the distance between adjacent grid points is checked, and if the largest arc-length distance exceeds the threshold, a redistribution of the grid points is triggered. First, the interface is rediscretized into N equally spaced points based on arc-length. The new x_F and y_F coordinates are interpolated from the current grid points using piecewise cubic Hermite interpolating polynomials [78]. Similarly, γ is interpolated at each point, with an additional factor applied. This factor ensures that the total circulation, or the arc-length integral of γ along the interface, remains unchanged before and after the redistribution.

V. NUMERICAL RESULTS AND DISCUSSION

Prior to presenting the simulation results and comparing them to the experiments, it is essential to reconcile a gap that exists between the two approaches. This gap is the inconsistency in the definition of the Froude number, or more fundamentally, the difference in the relationship between the three parameters that capture the nature of a vortex ring: the circulation Γ, the ring diameter L_0, and the propagation speed U. For a 3D circular vortex ring [79–81], U is known to be of the form

$$U \approx \frac{\Gamma}{2\pi L_0}\left[\ln\left(\frac{8L_0}{a}\right) - \frac{1}{4}\right], \tag{14}$$

where a is the diameter of the vortex core shown in Fig. 1(c). This will be referred to as the "3D model." However, U in the 2D point vortex model used in the simulations follows a different expression:

$$U = \frac{\Gamma}{2\pi L_0}. \tag{15}$$

This will be referred to as the "2D model." If the same vortex ring is to be correctly represented by these two different models, the logical approach is to assign the macroscopic quantities propagation speed U and diameter L_0 as intrinsic quantities, while allowing the circulation Γ to be different. This ensures that the motion and size of the vortex ring remains consistent across both models. Figure 9(a) shows the dependence of Γ on U for both the 2D and the 3D models for the vortex rings tested in the current experiment. The circulation measured directly by the experiment using PIV is also plotted. The 3D model captures the relation between the circulation and the propagation speed well, but there is a noticeable discrepancy between the values calculated using the 2D and 3D models. Consequently, when using the definition $\mathrm{Fr} = \Gamma/\sqrt{gL_0^3}$, the value of the Froude number for the same vortex ring in the 2D model differs from that in both the 3D model and the 3D experiment. This explains why, in some previous studies, such as in the work of Willmarth *et al.* [41] where a 2D model was employed, the vortex ring still dissipates at $\mathrm{Fr} > 1$. Therefore, to make a sensible comparison between the experimental and 2D simulation results, a transformed Froude number is

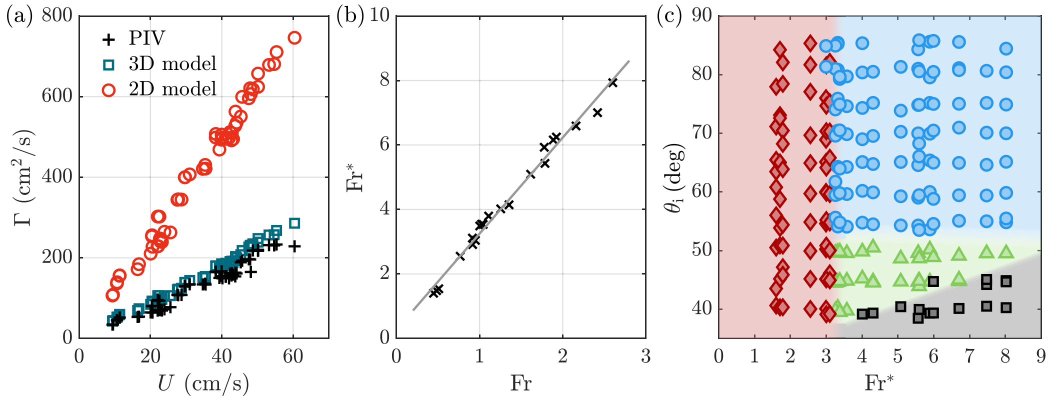

FIG. 9. Circulation Γ and Froude number Fr in 2D and 3D models are different for the same vortex ring. (a) Circulation versus the measured speed U. The cross symbols show Γ measured directly by PIV, the squares show Γ calculated by Eq. (14) using the measured speed U, while the circles show Γ calculated with the same U using Eq. (15). The 3D model closely matches the direct measurements, while the 2D model deviates from both, resulting in different values of Fr for the same vortex ring in the experiment and the 2D model we use. (b) The correspondence between the Froude number Fr and the transformed Froude number Fr*. The gray line is a linear fit. (c) The transformed phase diagram, from Fr $-$ θ_{i} space shown in Fig. 4 to that in Fr* $-$ θ_{i} space.

defined:

$$\mathrm{Fr}^* = \frac{2\pi U}{\sqrt{gL_0}}. \tag{16}$$

This takes the same value for the same vortex ring described by both the 2D and 3D models. Figure 9(b) shows the transition from the original Froude number Fr to the corresponding Fr* in Eq. (16). Naturally, Fr* takes on a greater value. The relationship between the two is approximately linear here, as both the L_0 and a remain relatively constant across the tested cases. Figure 9(c) shows the same phase diagram as Fig. 4 from the experiments, but with the transformed Froude number Fr*. The critical Froude number for reflection shifts to approximately 3.3.

A. Four types of behavior and associated interface deformations

Figure 10 shows typical examples of the same four vortex-pair behaviors as observed in the experiments. Although the same nomenclature is used to describe the phenomena observed in the simulations, the vortex pair does not numerically dissipate or break in the simulations. For each case in Fig. 10, the interface deformations are also shown in progressively darker shades of blue as time increases. Three time snapshots are plotted for each case, with the corresponding vortex pair shown in the same color.

As shown in Fig. 10(a), at small Fr*, the trajectories of both point vortices curve upward and the vortex pair rotates counterclockwise. The interface only deforms to a small extent near the upper point vortex, but otherwise remains mostly flat. Both the trajectories and interface deformation share the same features of the "dissipated" case observed in the experiments in Sec. II. Similar dynamics were obtained by Yu and Tryggvason [50] for the interaction of a free surface with a vortex pair incident at an angle of 45°. The simulations can terminate in one of the following two scenarios besides been manually stopped: either the GMRES solver fails to converge due to the development of nonphysical distortions and self-entanglement of the interface, or the distance between the two point vortices drops below a threshold, beyond which the vortex pair itself is deemed nonphysical. The former usually occurs when $\mathrm{Fr}^* \to 0$, whereas the latter when $\mathrm{Fr}^* \to \mathrm{Fr}^*_{\mathrm{c}}$, where $\mathrm{Fr}^*_{\mathrm{c}}$ denotes a critical Froude number above which a different mode of interaction occurs. A vortex pair is classified

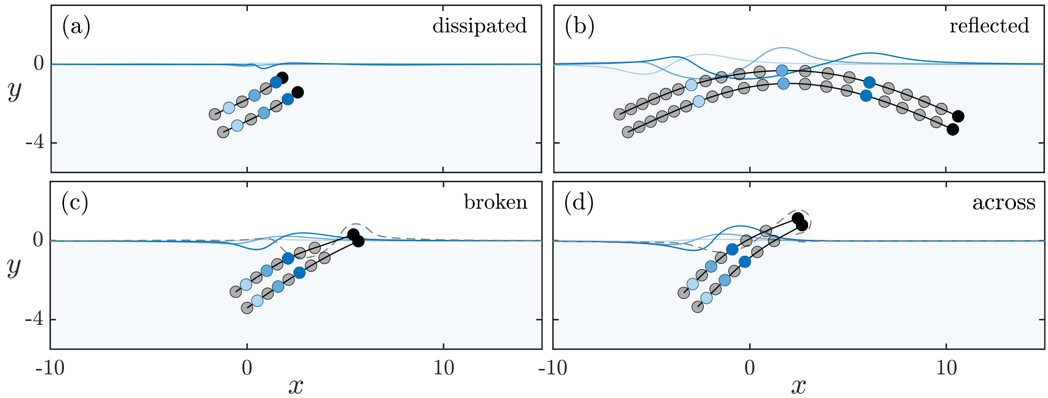

FIG. 10. Typical dynamics captured by the simulations, covering the four regimes observed in experiments. The parameters used are (a) $\mathrm{Fr}^* = 2$, $\theta_\mathrm{i} = 65^\circ$, (b) $\mathrm{Fr}^* = 8$, $\theta_\mathrm{i} = 65^\circ$, (c) $\mathrm{Fr}^* = 5$, $\theta_\mathrm{i} = 55^\circ$, and (d) $\mathrm{Fr}^* = 8$, $\theta_\mathrm{i} = 45^\circ$. In each case, three moments of the vortex pair and the corresponding interface are marked in blue, with different shades. Black dots show the last moment of each run. In panels (c) and (d), the interface at the last moment of each run is depicted by dashed gray curves. For the complete movies see the Supplemental Material [66].

as "dissipated," if the simulation terminates in one of these scenarios while both point vortices remain below the interface.

The interface deformations and the vortex pair trajectory of another case shown in Fig. 10(b) share the same main features as the "reflected" cases obtained in experiments. The simulations proceed stably until they are terminated manually after rendering a full reflection trajectory. As the vortex pair approaches, it pushes the interface upward, with the maximum elevation occurring directly above, while simultaneously generating vorticity on the interface. The significant interface elevation, combined with the vorticity generated at the interface, is the key mechanism responsible for the horizontal velocity difference between the upper and lower cores of the vortex ring, thereby inducing reflection. The difference in the horizontal velocity of the two point vortices can be seen from Eq. (4), by considering the real part of $\mathrm{d}\bar{z}_1/\mathrm{d}t - \mathrm{d}\bar{z}_2/\mathrm{d}t$, which yields

$$\Delta u_x := \frac{\mathrm{d}x_1}{\mathrm{d}t} - \frac{\mathrm{d}x_2}{\mathrm{d}t} = -\frac{1}{2\pi}\int_{-\infty}^{\infty} \gamma(e,t)\frac{y_1(t) - y_F(e,t)}{[x_1(t) - x_F(e,t)]^2 + [y_1(t) - y_F(e,t)]^2}\,\mathrm{d}e$$
$$+\frac{1}{2\pi}\int_{-\infty}^{\infty} \gamma(e,t)\frac{y_2(t) - y_F(e,t)}{[x_2(t) - x_F(e,t)]^2 + [y_2(t) - y_F(e,t)]^2}\,\mathrm{d}e. \qquad (17)$$

The premises are that $|\gamma(e)|$ increases as the vortex pair approaches the interface and $|\gamma(e)|$ diminishes in the region where $|x_{1,2} - x_F|$ is large. Then based on Eq. (17), the influence of the interface decays with the distance between the point vortices and the interface, and the influence on the velocity of the point vortices from the region directly above the vortex pair is dominant. Thus, at a given point in time, Eq. (17) can be approximated by

$$\Delta u_x \approx \frac{1}{2\pi}\int_{e_0-\Delta e}^{e_0+\Delta e} \gamma(e)\left[-\frac{1}{y_1 - y_F(e)} + \frac{1}{y_2 - y_F(e)}\right]\mathrm{d}e, \qquad (18)$$

where Δe gives a small interval $(x_F(e_0 - \Delta e), x_F(e_0 + \Delta e))$ near x_1 and x_2, such that $|x_F - x_{1,2}| < \Delta x$, and $|y_{1,2} - y_F|$ is always large compared to Δx. In this form, the contributions from the regions with large $|x_F - x_{1,2}|$ are ignored, and the terms $y_{1,2} - y_F$ dominate the denominators in Eq. (17) in the region where $|x_F - x_{1,2}|$ is small. Although this is an oversimplification, it can still provide some insights into the mechanism. Equation (18) further simplifies to

$$\Delta u_x \approx \frac{1}{2\pi}\int_{e_0-\Delta e}^{e_0+\Delta e} \gamma(e)\frac{y_1 - y_2}{[y_1 - y_F(e)][y_2 - y_F(e)]}\,\mathrm{d}e. \tag{19}$$

With a given incident angle, $y_1 - y_2$ does not vary significantly. In addition, the simulations show that $\gamma(e)$ is positive in the interval $(e_0 - \Delta e, e_0 + \Delta e)$. Thus, Δu_x is always positive and increases as $\gamma(e)$ increases. At the same time, as the vortex pair approaches the interface, $(y_1 - y_F)(y_2 - y_F)$ decreases which also causes Δu_x to increase. A similar argument can be used to explain why Δu_x decreases as the vortex pair travels away from the interface. In the meantime, the difference in the vertical velocities of the two point vortices in the vortex pair can be approximated by

$$\Delta u_y \approx \frac{1}{2\pi}\int_{e_0-\Delta e}^{e_0+\Delta e} \gamma(e)\frac{x_1 - x_F(e)}{[y_1 - y_F(e)]^2}\,\mathrm{d}e - \frac{1}{2\pi}\int_{e_0-\Delta e}^{e_0+\Delta e} \gamma(e)\frac{x_2 - x_F(e)}{[y_2 - y_F(e)]^2}\,\mathrm{d}e. \tag{20}$$

The integrals in the above equation evaluate to negligible values due to the near odd symmetry of the integrands about e_0. Then the vertical velocity difference between the point vortices is always small. This explains the velocity decomposition shown in Figs. 6(a) and 6(b). Overall, this difference in the horizontal velocities of the two point vortices, coupled with the similarity in their vertical velocities, leads to the rotation of the vortex pair. This rotation ultimately causes the vortex pair to reflect off the interface, as observed in both the experiments and the numerical simulations.

The parameters ($\mathrm{Fr}^*, \theta_\mathrm{i}$) used in Figs. 10(c) and 10(d) are $(5, 55^\circ)$ and $(8, 45^\circ)$, respectively. In these cases, the trajectories curve down initially, similar to the reflected case in Fig. 10(b). The interface deformation is also wavelike. Then the point vortices go above the $y = 0$ line and the interface deformation turns into a blunt bump or jet shape for the broken and across behavior, respectively, as shown by the dashed gray lines. Meanwhile, the distance between the two point vortices shrinks which causes the simulation to terminate, mirroring the vortex ring breakup observed at the interface in the experiments.

B. The phase diagram produced from the model

The simulations also provide a similar phase diagram in the Fr^* and θ_i space, presented in Fig. 11(a), that encompasses the four types of phenomena observed in the experiments. Despite the simplicity of the model, the primary dynamics and their corresponding regions in $\mathrm{Fr}^* - \theta_\mathrm{i}$ space show good agreement with the experimental results in Sec. III. "Dissipated" vortex pairs are observed at small Fr^* with any θ_i, and reflected vortex pairs exist above a critical Fr^*_c and critical θ_c that is approximately 4 and 55°, respectively. The "across" behavior takes up the whole regime for large Fr^* ($\gtrsim 4$) and small θ_i ($<55^\circ$). This is due to the inviscid nature of the model which eliminates the effects that lead to the breakup of the vortex pair, such as air entrainment and instability development. However, several "broken" cases still occur in the central region where the three regimes intersect. This is due to the sensitivity of the criteria used to classify cases at the boundaries of the regimes. A slight change in the criterion parameter can lead to a slightly different classification of the results, but only near the boundaries of the different regimes, where the distinction is subtle. Despite this, the physical picture of the three main regimes is consistent with the experimental results. In addition, the detailed features of the reflection behavior are also well captured by the model. The angle evolution for the rotation of the "reflected" vortex pairs at different incident angles is shown in Fig. 11(b). Similar to Fig. 5(c) obtained from the experiments, $|\theta(x)|$ starts with the incident angle θ_i and increases up to 90° as the vortex pair approaches the interface. Then $|\theta(x)|$ starts to decrease, and eventually reaches a value that is slightly smaller than the incident angle θ_i.

In summarizing this section, the 2D vortex sheet and vortex pair model captures both the phase diagram and the detailed features of the reflection phenomenon, including the slight asymmetry in the angular evolution of the vortex ring, as observed in the experiments. A detailed analysis of the governing equations that comprise the model, provides valuable insights into the mechanism of

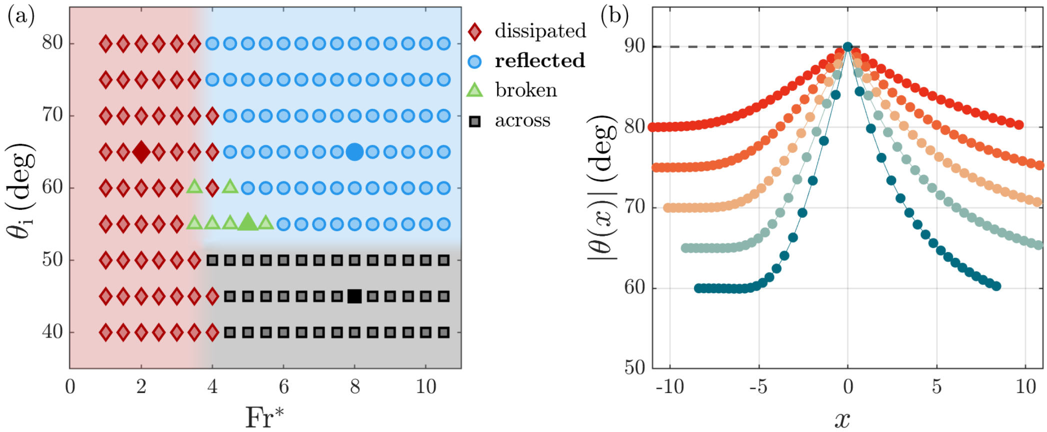

FIG. 11. Simulation results. (a) Phase diagram of the interactions between the vortex pair and the free interface in $\mathrm{Fr}^* - \theta_i$ space, obtained from numerical simulations. The four solid, larger markers correspond to the four cases shown in Fig. 10. (b) The propagation angle $|\theta(x)|(^\circ)$ of the vortex pair at different x positions during the reflection when $\mathrm{Fr}^* = 8$. Similar to the experimental data shown in Fig. 5(c), each $|\theta(x)|$ changes from θ_i to 90° and then drops back after reflection, showing the rotation of the vortex pair.

vortex ring reflection. A more detailed description of the surface and vortical structure evolutions can only be given by employing more sophisticated 3D simulations. Some possible methods are discussed in previous works [53,56,67].

VI. SIMPLE MASS CONSERVATION MODEL

The above 2D vortex-sheet-vortex-pair model has successfully captured the essential dynamics observed in the experiments. In order to gain an intuitive understanding of the interaction between vortex rings and a free interface, we introduce a simple model based on the flux conservation for each portion of the advancing ring. In this model, the upper and lower portions of the same 3D vortex ring are treated separately, but the vortex velocity is determined by both. That is, the velocity vector is always perpendicular to the line connecting the two cores. In the fluid bulk far from the interface, both cores move forward at the same rate; their connecting line translates along a straight line, normal to the vortex velocity. However, in a situation depicted in Fig. 12(a), the upper core experiences a narrow passage ahead of its path. Flux or mass conservation requires the upper core to accelerate, more so if the passage is smaller. Here, the simple rule is as follows: the product of the core speed and the area it occupies (a rectangular box) in water, which is the local flux for each core, remains constant $v_0 A_0$. The areas A_1 and A_2 represent the fluid volumes entrained by each core, and also serve the dual purpose as fluid passages. The same rule applies to both cores. As a result, at each time step while moving forward, the upper core accelerates more significantly than the lower core. Over time, the upper core passes the lower one. The orientation of the connecting line between the two cores gradually changes clockwise, leading to the reflection of the vortex ring, as shown in Fig. 12(b).

Both box areas A_1 and A_2 are shown in Fig. 12(a). When the vortex ring is close to the interface, at least the upper box is truncated in size. Considering the fact that the interface tends to remain flat, the following equation must be satisfied for the conservation of mass flux for an incompressible fluid:

$$v_k^n A_k^n = v_0 A_0 \quad \text{for } k = 1, 2, \tag{21}$$

with v_0 representing the propagation speed U and A_0 the initial box area. At $t = 0$ we assume that $v_1^0 = v_2^0 = v_0$ and $A_1^0 = A_2^0 = A_0$, and both boxes are fully immersed in the water. The two cores are

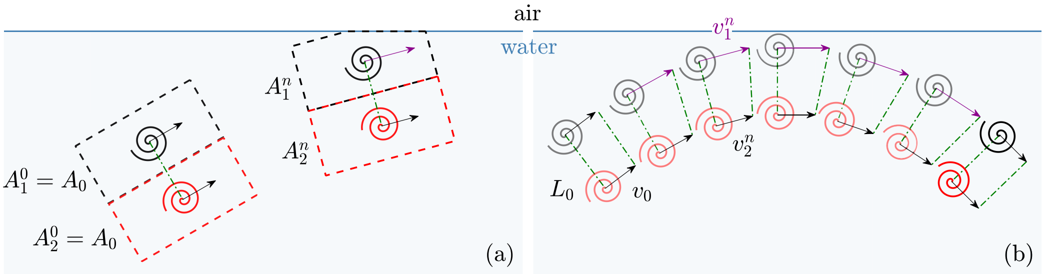

FIG. 12. A flux conservation model explains the velocity difference between the upper and lower cores, and hence the reflection. The velocities of the two cores are considered separately, with a flow channel or passage assigned to each of them, shown by the dashed areas with an initial area A_0. When the two cores propagate forward, area A_0 sees the same passage, thus maintains its original speed. When moving closer to the interface, the channel for the upper core will be truncated, for instance, to A_1^n. Then the upper core must speed up to satisfy the requirement $v_1^n A_1^n = v_2^n A_2^n = v_0 A_0$, which results in a velocity difference and the reorientation of the vortex ring. Gradually, the vortex is reflected.

placed at the centers of their respective box whose width is chosen as the initial separation between the two cores, L_0. The two cores are evolved by updating their positions and velocities as follows: at each time step the area of the box below the interface is checked. If any part of a box crosses the interface, its area A_k^n is updated to be the area of the new emergent polygon, which is the rectangle after truncation. Once A_k^n is determined, v_k^n is updated according to Eq. (21). The results of this simple mass conservation model are presented in Fig. 13 for $\theta_{\mathrm{i}} = 65^\circ$.

The velocity components of the two vortex cores are shown in Figs. 13(a) and 13(b). Figure 13(a) shows how the horizontal component of the velocity u_x, of each core, changes versus the horizontal spatial coordinate x, as predicted by the model (solid and dashed lines). As the vortex cores approach the interface, the upper core experiences a larger u_x increase than the lower core. Figure 13(b) instead shows how the vertical component of the velocity u_y changes as the vortex cores propagate. In this case, the two cores have almost identical u_y throughout the process. The value of

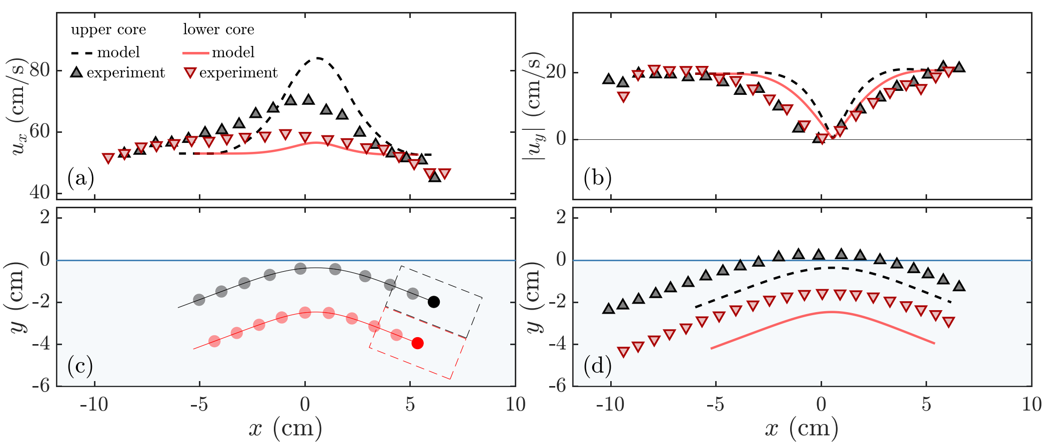

FIG. 13. Comparison between the model and experimental results, showing that the simple model captures the reflection behavior. (a) The model-predicted horizontal velocity u_x for the two cores (curves) and the corresponding experimental result (triangles); (b) the vertical component $|u_y|$ are shown using the same symbols. (c) The trajectories of the vortex cores predicted by the model. (d) Comparison between the trajectories from (c) and the experimental results, in $x - y$ space.

$u_y = 0$ corresponds to an instant when the vortex ring moves parallel to the water-air interface. After that, u_y increases again, showing a change in direction when the vortex ring is reflected by the interface. The vortex trajectories predicted by the model are shown in Fig. 13(c). The flat blue line at $y = 0$ is the water-air interface. The two curves show the traces of the upper and lower cores, respectively. The circles show snapshots at equal time intervals before and after the reflection. This model captures the reflection qualitatively and a comparison with experiments is presented in Fig. 13(d).

In summary, the simple model presented in this section is reminiscent of the Huygens-Fresnel principle that explains wave propagation [82], in that different parts of a vortex collectively determine its direction of travel. It effectively describes the reflection of the vortex ring at the interface. It also helps to explain why horizontally issued vortex rings are deflected when they start at a distance close to the free interface (Fig. 7). In that case, the upper portion of a vortex ring has a narrow passage to advance, so it has to accelerate, given its initial momentum. When the free interface is replaced by a solid wall, the no-slip boundary condition imposed on the upper core introduces significant dissipation, breaking a speeding core. This effect is not part of the simple model. At sufficiently small incident angles, the model would show that one or both cores accelerate and move above the interface, ending with a situation where the core speed diverges. This corresponds to a "broken" or "across" case. Although further refinement of the model is needed to predict quantities such as the critical incident angle, this toy model undoubtedly provides some intuition on the phenomenon.

VII. DISCUSSION AND CONCLUSIONS

In this work, we study how vortex rings interact with a free water-air interface. Through systematic experimentation, a phase diagram is constructed that demonstrates four different behaviors. These behaviors include the so-called dissipated, reflected, broken, and across cases. The phase diagram is divided into three regimes delineated by critical values of the Froude number $\mathrm{Fr_c} \simeq 1$ and incident angle θ_c ($53 \sim 55$ degrees). When $\mathrm{Fr} < \mathrm{Fr_c}$, the vortex ring dissipates regardless of the incident angle. For $\mathrm{Fr} \geqslant \mathrm{Fr_c}$, the vortex ring reflects at $\theta_i \geqslant \theta_c$, as the vortex ring gradually turns around when it moves close to the interface. Before and after the reflection, the change in the speed of the vortex ring is small and the incident and exiting angles are essentially the same, leading to symmetric reflections. When $\theta_i < \theta_c$ and $\mathrm{Fr} \geqslant \mathrm{Fr_c}$, the vortex ring crosses or breaks up at the interface, depending on the specific value of the Froude number.

Our numerical simulations using the vortex sheet and vortex pair model provide a similar phase diagram. The model gives values of both the critical Froude number and critical incident angle for reflection, closely aligned with the experimental results. From both the experiments and simulations, the reflection is seen to be accompanied by the gradual reorientation of the vortex ring. During this process, the speed of the upper core exceeds that of the lower core because of the influence of the boundary. Detailed analysis of the governing equations of the vortex sheet and vortex pair model shows that the interface induces a larger velocity to the upper core as it is closer than the lower one. The toy model, which considers the local flux conservation, also explains the speed difference.

Physically, the free interface plays the role of an elastic spring, which stores energy through its temporally deformed shape. The deformation and subsequent restoration of the interface during reflection shows the exchange between the kinetic energy of the vortex ring and the energy associated with the deformed interface. The vertical kinetic energy of the vortex ring creates a bump over the original flat interface, which has a higher potential energy than before, and a curved surface that has an extra surface energy. Both energies tend to minimize spontaneously, converting back to the moving vortex ring. This picture is consistent with the observation that there is no reflection when the free interface is replaced by a solid boundary: no energy can be stored. However, such an energy-storing-and-releasing mechanism has a limit. When the interface is further deformed, as the incident angle is sufficiently small and Fr high, the water bump develops into a jet in the air. The energy conversion mechanism is no longer reversible. In such cases, the integrity of the vortex ring is also destroyed.

Through experimental investigation, numerical simulations, and detailed analysis, we have expanded the understanding of how vortex rings interact with a free boundary—the water-air interface, particularly in cases with large Froude numbers. Future work could focus on providing a theoretical explanation for the critical values of the Froude number or conducting 3D simulations to reveal more details on the vortical structure and interface evolutions. Additionally, the similarity between the reflection phenomenon of vortex rings and the total internal reflection of light merits further exploration.

ACKNOWLEDGMENTS

We thank Michael Shelley for many helpful discussions. C.M. acknowledges funding support provided by a Courant Instructorship and Joseph B. Keller Postdoctoral Fellowship at the Courant Institute at NYU. J.Z. acknowledges support from the National Natural Science Foundation of China, under Grant No. NSFC92252204.

J.Z. designed the research and came up with the toy model; Z.S. performed the experiment and simulated the vortex sheet model and the toy model; C.M. refined the vortex sheet model and performed the simulations. All three authors wrote the manuscript together.

DATA AVAILABILITY

The data that support the findings of this article are not publicly available. The data are available from the authors upon reasonable request.

[1] H. Helmholtz, Über Integrale der hydrodynamischen Gleichungen, welche den Wirbelbewegungen entsprechen, J. Reine Angewand. Math. **1858**, 25 (1858).
[2] H. Kragh, The vortex atom: A Victorian theory of everything, Centaurus **44**, 32 (2002).
[3] W. Thomson, II. On vortex atoms, London Edinburgh Dublin Philos. Mag. J. Sci. **34**, 15 (1867).
[4] W. Thomson, XLV. On the propagation of laminar motion through a turbulently moving inviscid liquid, London Edinburgh Dublin Philos. Mag. J. Sci. **24**, 342 (1887).
[5] M. R. Dennis, R. P. King, B. Jack, K. O'Holleran, and M. J. Padgett, Isolated optical vortex knots, Nat. Phys. **6**, 118 (2010).
[6] W. T. M. Irvine and D. Bouwmeester, Linked and knotted beams of light, Nat. Phys. **4**, 716 (2008).
[7] H. K. Moffatt, The degree of knottedness of tangled vortex lines, J. Fluid Mech. **35**, 117 (1969).
[8] D. Kleckner and W. T. M. Irvine, Creation and dynamics of knotted vortices, Nat. Phys. **9**, 253 (2013).
[9] M. W. Scheeler, D. Kleckner, D. Proment, G. L. Kindlmann, and W. T. M. Irvine, Helicity conservation by flow across scales in reconnecting vortex links and knots, Proc. Natl. Acad. Sci. USA **111**, 15350 (2014).
[10] P. G. Tait, IV. Listing's topologie, London Edinburgh Dublin Philos. Mag. J. Sci. **17**, 30 (1884).
[11] J. Przytycki, Classical roots of knot theory, Chaos Solitons Fractals **9**, 531 (1998).
[12] M. Epple, Topology, matter, and space, I: Topological notions in 19th-century natural philosophy, Arch. Hist. Exact Sei. **52**, 297 (1998).
[13] T. Matsuzawa, N. P. Mitchell, S. Perrard, and W. T. M. Irvine, Creation of an isolated turbulent blob fed by vortex rings, Nat. Phys. **19**, 1193 (2023).
[14] J. Yao and F. Hussain, Vortex reconnection and turbulence cascade, Annu. Rev. Fluid Mech. **54**, 317 (2022).
[15] F. Pulvirenti, S. Scollo, C. Ferlito, and F. M. Schwandner, Dynamics of volcanic vortex rings, Sci. Rep. **13**, 2369 (2023).
[16] O. V. Fuentes, Early observations and experiments on ring vortices, Eur. J. Mech. B Fluids **43**, 166 (2014).

[17] P. F. Linden and J. S. Turner, 'Optimal' vortex rings and aquatic propulsion mechanisms, Proc. R. Soc. London B **271**, 647 (2004).
[18] P. M. Arvidsson, S. J. Kovács, J. Töger, R. Borgquist, E. Heiberg, M. Carlsson, and H. Arheden, Vortex ring behavior provides the epigenetic blueprint for the human heart, Sci. Rep. **6**, 22021 (2016).
[19] C. Cummins, M. Seale, A. Macente, D. Certini, E. Mastropaolo, I. M. Viola, and N. Nakayama, A separated vortex ring underlies the flight of the dandelion, Nature (London) **562**, 414 (2018).
[20] C. Donnelly, K. L. Metlov, V. Scagnoli, M. Guizar-Sicairos, M. Holler, N. S. Bingham, J. Raabe, L. J. Heyderman, N. R. Cooper, and S. Gliga, Experimental observation of vortex rings in a bulk magnet, Nat. Phys. **17**, 316 (2021).
[21] C. Wan, Q. Cao, J. Chen, A. Chong, and Q. Zhan, Toroidal vortices of light, Nat. Photon. **16**, 519 (2022).
[22] E. F. Northrup, An experimental study of vortex motions in liquids, J. Franklin Inst. **172**, 211 (1911).
[23] E. F. Northrup, A photographic study of vortex rings in liquids, Nature (London) **88**, 463 (1912).
[24] C. Tung and L. S. Ting, Motion and decay of a vortex ring, Phys. Fluids **10**, 901 (1967).
[25] P. G. Saffman, The velocity of viscous vortex rings, Stud. Appl. Math. **49**, 371 (1970).
[26] L. E. Fraenkel, On steady vortex rings of small cross-section in an ideal fluid, Proc. R. Soc. London A **316**, 29 (1970).
[27] T. Maxworthy, The structure and stability of vortex rings, J. Fluid Mech. **51**, 15 (1972).
[28] J. Norbury, A family of steady vortex rings, J. Fluid Mech. **57**, 417 (1973).
[29] A. Glezer and D. Coles, An experimental study of a turbulent vortex ring, J. Fluid Mech. **211**, 243 (1990).
[30] A. Weigand and M. Gharib, On the evolution of laminar vortex rings, Exp. Fluids **22**, 447 (1997).
[31] Y. Fukumoto and Y. Hattori, Curvature instability of a vortex ring, J. Fluid Mech. **526**, 77 (2005).
[32] I. S. Sullivan, J. J. Niemela, R. E. Hershberger, D. Bolster, and R. J. Donnelly, Dynamics of thin vortex rings, J. Fluid Mech. **609**, 319 (2008).
[33] T. Fohl and J. S. Turner, Colliding vortex rings, Phys. Fluids **18**, 433 (1975).
[34] Y. Oshima and S. Asaka, Interaction of multi-vortex rings, J. Phys. Soc. Jpn. **42**, 1391 (1977).
[35] S. Kida, M. Takaoka, and F. Hussain, Reconnection of two vortex rings, Phys. Fluids **1**, 630 (1989).
[36] M. V. Melander and F. Hussain, Cross-linking of two antiparallel vortex tubes, Phys. Fluids **1**, 633 (1989).
[37] T. T. Lim and T. B. Nickels, Instability and reconnection in the head-on collision of two vortex rings, Nature (London) **357**, 225 (1992).
[38] J. D. A. Walker, C. R. Smith, A. W. Cerra, and T. L. Doligalski, The impact of a vortex ring on a wall, J. Fluid Mech. **181**, 99 (1987).
[39] T. T. Lim, An experimental study of a vortex ring interacting with an inclined wall, Exp. Fluids **7**, 453 (1989).
[40] T. H. New, J. Long, B. Zang, and S. Shi, Collision of vortex rings upon V-walls, J. Fluid Mech. **899**, A2 (2020).
[41] W. W. Willmarth, G. Tryggvason, A. Hirsa, and D. Yu, Vortex pair generation and interaction with a free surface, Phys. Fluids **1**, 170 (1989).
[42] L. P. Bernal and J. T. Kwon, Vortex ring dynamics at a free surface, Phys. Fluids **1**, 449 (1989).
[43] S. Ohring and H. J. Lugt, Interaction of an obliquely rising vortex ring with a free surface in a viscous fluid, Meccanica **31**, 623 (1996).
[44] YouTube videos on vortex rings, https://www.youtube.com/watch?v=oEt1Bf3P5ZM and https://www.youtube.com/watch?v=EnYhp3xB7Xo.
[45] C. C. Chu and R. E. Falco, Vortex ring/viscous wall layer interaction model of the turbulence production process near walls, Exp. Fluids **6**, 305 (1988).
[46] K. Kuehn, M. Moeller, M. Schulz, and D. Sanfelippo, Vortex ring refraction at large Froude numbers, Phys. Rev. E **82**, 016312 (2010).
[47] M. M. Cawte, X. Yu, B. Anderson, and A. Bradley, Snell's law for a vortex dipole in a Bose-Einstein condensate, SciPost Phys. **6**, 032 (2019).
[48] J. G. Telste, Potential flow about two counter-rotating vortices approaching a free surface, J. Fluid Mech. **201**, 259 (1989).
[49] L. P. Bernal, A. Hirsa, J. T. Kwon, and W. W. Willmarth, On the interaction of vortex rings and pairs with a free surface for varying amounts of surface active agent, Phys. Fluids **1**, 2001 (1989).

[50] D. Yu and G. Tryggvason, The free-surface signature of unsteady, two-dimensional vortex flows, J. Fluid Mech. **218**, 547 (1990).

[51] M. Song, L. P. Bernal, and G. Tryggvason, Head-on collision of a large vortex ring with a free surface, Phys. Fluids **4**, 1457 (1992).

[52] H. J. Lugt and S. Ohring, The oblique rise of a viscous vortex ring toward a deformable free surface, Meccanica **29**, 313 (1994).

[53] C. Wu, Q. Fu, and H. Ma, Interactions of three-dimensional viscous axisymmetric vortex rings with a free surface, Acta Mechanica Sinica **11**, 289 (1995).

[54] A. Weigand and M. Gharib, Turbulent vortex ring/free surface interaction, J. Fluids Eng. **117**, 374 (1995).

[55] M. Gharib and A. Weigand, Experimental studies of vortex disconnection and connection at a free surface, J. Fluid Mech. **321**, 59 (1996).

[56] C. Zhang, L. Shen, and D. K. P. Yue, The mechanism of vortex connection at a free surface, J. Fluid Mech. **384**, 207 (1999).

[57] P. J. Archer, T. G. Thomas, and G. N. Coleman, The instability of a vortex ring impinging on a free surface, J. Fluid Mech. **642**, 79 (2010).

[58] H. von Helmholtz, LXIII. On integrals of the hydrodynamical equations, which express vortex-motion, London Edinburgh Dublin Philos. Mag. J. Sci. **33**, 485 (1867).

[59] K. Shariff and A. Leonard, Vortex rings, Annu. Rev. Fluid Mech. **24**, 235 (1992).

[60] L. Gan, J. R. Dawson, and T. B. Nickels, On the drag of turbulent vortex rings, J. Fluid Mech. **709**, 85 (2012).

[61] N. Didden, On the formation of vortex rings: Rolling-up and production of circulation, Z. angewand. Math. Phys. (ZAMP) **30**, 101 (1979).

[62] J. O. Dabiri and M. Gharib, Fluid entrainment by isolated vortex rings, J. Fluid Mech. **511**, 311 (2004).

[63] F. W. Roos and W. W. Willmarth, Some experimental results on sphere and disk drag, AIAA J. **9**, 285 (1971).

[64] T. Maxworthy, Turbulent vortex rings, J. Fluid Mech. **64**, 227 (1974).

[65] K. C. Stewart, C. L. Niebel, S. Jung, and P. P. Vlachos, The decay of confined vortex rings, Exp. Fluids **53**, 163 (2012).

[66] See Supplemental Material at http://link.aps.org/supplemental/10.1103/dg4m-hbts for additional experimental data, derivations of the governing equations, and a caption list for the supplemental movies.

[67] R. Camassa, S. Khatri, R. McLaughlin, K. Mertens, D. Nenon, C. Smith, and C. Viotti, Numerical simulations and experimental measurements of dense-core vortex rings in a sharply stratified environment, Comput. Sci. Disc. **6**, 014001 (2013).

[68] R. Camassa, D. M. Harris, D. Holz, R. M. McLaughlin, K. Mertens, P.-Y. Passaggia, and C. Viotti, Variable density vortex ring dynamics in sharply stratified ambient fluids, Phys. Rev. Fluids **1**, 050503 (2016).

[69] Y. Su, M. M. Wilhelmus, and R. Zenit, Asymmetry of motion: Vortex rings crossing a density gradient, J. Fluid Mech. **960**, R1 (2023).

[70] J. Pinaud, J. Albagnac, S. Cazin, Z. Rida, D. Anne-Archard, and P. Brancher, Three-dimensional measurements of an inclined vortex ring interacting with a density stratification, Phys. Rev. Fluids **6**, 104701 (2021).

[71] G. R. Baker, D. I. Meiron, and S. A. Orszag, Generalized vortex methods for free-surface flow problems, J. Fluid Mech. **123**, 477 (1982).

[72] G. R. Baker, D. I. Meiron, and S. A. Orszag, Generalized vortex methods for free surface flow problems. II: Radiating waves, J. Sci. Comput. **4**, 237 (1989).

[73] G. Tryggvason, Deformation of a free surface as a result of vortical flows, Phys. Fluids **31**, 955 (1988).

[74] M. J. Shelley and M. Vinson, Coherent structures on a boundary layer in Rayleigh-Benard turbulence, Nonlinearity **5**, 323 (1992).

[75] R. Krasny, Desingularization of periodic vortex sheet roll-up, J. Comput. Phys. **65**, 292 (1986).

[76] R. Krasny, Computation of vortex sheet roll-up in the Trefftz plane, J. Fluid Mech. **184**, 123 (1987).

[77] Y. Saad and M. H. Schultz, GMRES: A generalized minimal residual algorithm for solving nonsymmetric linear systems, SIAM J. Sci. Stat. Comput. **7**, 856 (1986).

[78] The MathWorks Inc, MATLAB version: R2024b, Piecewise Cubic Hermite Interpolating Polynomial (PCHIP) function (2024), https://fr.mathworks.com/help/matlab/ref/double.interp1.html.
[79] Lord Kelvin, The translatory velocity of a circular vortex ring, Philos. Mag. **33**, 511 (1867).
[80] P. G. Saffman, *Vortex Dynamics* (Cambridge University Press, New York, 1992).
[81] J.-Z. Wu, H.-Y. Ma, and M.-D. Zhou, *Vorticity and Vortex Dynamics* (Springer Science & Business Media, New York, 2007).
[82] R. W. Wood, *Physical Optics* (Macmillan, New York, 1905).